

Optimizing fluid mixing in channel flow using wall-mounted flexible structures

Gaurav Singh^{a,*}, Arahata Senapati^a, Arnab Atta^b and Rajaram Lakkaraju^{c,**}

^aAdvanced Technology and Development Centre, Indian Institute of Technology Kharagpur, West Midnapore, 721302, W.B., India

^bDepartment of Chemical Engineering, Indian Institute of Technology Kharagpur, West Midnapore, 721302, W.B., India

^cTuRbulent Interfaces And Dispersion (TRIAD) Group, Department of Mechanical Engineering, Indian Institute of Technology Kharagpur, West Midnapore, 721302, W.B., India

ARTICLE INFO

Keywords:

fluid mixing
fluid structure interaction
flow transition
flexible structures
vortex generation
mixing performance

ABSTRACT

In channel mixers with two parallel streams of fluid, mixing is achieved by either laminar diffusion at low Reynolds numbers or from flow agitation due to geometric variations. Traditionally, rigid obstructions or textures are used in various spatial arrangements to improve fluid mixing. In our work, we have numerically investigated the mixing performance of a passive scalar in a two-dimensional channel flow accompanied by wall-mounted flexible plates as obstructions for a wide range of low Reynolds numbers (Re). The thin plates are arranged on opposite walls of the channel, and the distance between them is varied in the range $0h$ to $2h$, where h is the channel lateral width. The different arrangements result in corresponding flow paths, thereby affecting fluid mixing and flow rate due to the pressure head losses. We assessed the mixing performance in the channel via the mixing index and the head loss. Our results show that the channel with the two plates when arranged exactly opposite the walls (without a separation gap), offers the highest mixing with significant pressure drop. In contrast, either a single plate or two plates widely separated result in nearly similar levels of mixing index with a lower head loss. We devised a performance index based on a cost-benefit analogy by comparing the flexible plate configurations with the plane channel (i.e. without any obstruction) so as to assess the mixing effectiveness and found that a single flexible plate in the channel in the flow conditions with $Re \approx 400$ suit the best for the mixing of two fluid in the channel.

1. Introduction

Fluid mixing is a crucial process in various industries, such as fuel emulsification in petrochemicals, raw material blending in the food industry, and mixing chemical reagents (Yeh et al., 2015; Núñez-Flores et al., 2020; Peterwitz and Schembecker, 2021; Wang and Zhen, 2021). To achieve adequate mixing in channel flows, passive methods (like placing obstacles) and active methods (using externally powered actuators) can be employed. Passive methods, such as asymmetric grooves, rigid laminations, and serpentine channels, are simple and energy-efficient as they rely on the flow inertia (Nguyen and Wu, 2005; Yang et al., 2008; Afzal and Kim, 2014; Kashid et al., 2011; Kang, 2015; Derksen, 2010). Modifying the structural and dimensional aspects of

mixing channels can improve mixing outcomes by inducing chaotic convective motions. For instance, Yang et al. (2015) developed a channel design inspired by the three-dimensional Tesla design, demonstrating a robust mixing index of 0.97 (where 0 meant no-mixing and 1 meant perfect-mixing case) within a Reynolds number range of 0.1 to 100.

Instead of rigid laminations, the use of flexible plates involves complex interactions between hydrodynamic forces and structural responses, leading to various instabilities (Eloy et al., 2008; Zhang et al., 2001; Sadatoshi, 1968; Watanabe et al., 2002; Alben and Shelley, 2008). These instabilities trigger flow transition by generating eddies in the flow, causing significant improvement in fluid mixing (Singh and Lakkaraju, 2019; Rips and Mittal, 2019; Singh et al., 2024b). The incorporation of various vortex-generating methods in mixing channels has emerged as a key approach in enhancing the mixing process (Ali et al., 2015; Khatavkar et al., 2007; Dadvand et al., 2019; Ali et al., 2016; Hosseini et al., 2021; Ali et al., 2017; Evgren et al., 2011; Derksen, 2010;

*Corresponding author

**Principal corresponding author

E-mail addresses: thegauravonline@gmail.com (G. Singh); rajaram.lv@gmail.com (R. Lakkaraju)
ORCID(s):

Grosshans et al., 2015). In contrast, for rigid geometry-based vortex generators, the generated vortices primarily remain confined to the small wake region immediately behind the obstacle. This confinement leads to insufficient mixing near the channel walls, particularly when the channel dimensions significantly exceed the size of the obstacle (Wang et al., 2020). A promising solution to this limitation is to employ flexible structures as vortex generators (Hsiao et al., 2014; Park et al., 2019; Saleh et al., 2019; Zhao, 2020; Chen et al., 2020; Nazari et al., 2020; Singh et al., 2024a; Kakroo and Sadat, 2024). A crucial method within this approach involves the placement of the obstructions in the flow that act as catalysts for flow agitation (Abdelhamid et al., 2021; Yadav et al., 2021; Jing and Zhan, 2022; Yu et al., 2017). Earlier works (Huera-Huarte and Gharib, 2011; Borazjani and Sotiropoulos, 2009; Wang and Zhou, 2018) have investigated the flow features when two flexible circular cylinders are placed one after the other. Wang and Zhou (2018) showed that the two structures act as a single body when placed at small separation, resulting in entirely different flow features when placed at a certain distance. Such strategies have also been used to enhance fluid mixing (Ward and Fan, 2015) and slug mitigation processes (Mehendale et al., 2018).

While experimental methods can measure pressure loss in channel flows, capturing erratic flow and plate motions is challenging, making numerical simulations a preferred approach. Various numerical techniques have been employed in previous studies to simulate fluid-structure interaction problems. In context with the previous works on channel flows, we performed a two-dimensional numerical study to inspect fluid mixing in a channel flow containing two wall-mounted flexible plates mounted on opposite walls. We have systematically varied the position of the two plates to alter the flow features and quantify mixing using standard mixing metrics. We have also investigated the role of the flow Reynolds number that is best suited for efficient mixing conditions. Based on the strong coupling between the flow and the positioned structures, we aim to enhance mixing without causing significant pressure drop. We have focused our study on value (mixing) for cost (head loss) analogy and found the optimal configuration for mixing. In the following sections, we have discussed mathematical formulation, followed by our results and summary.

2. Methodology and computational setup

In Figure 1, we have shown a schematic of our model, a two-dimensional (2D) channel of height h and length $14h$ with two differently dyed fluid flows in the top half and the bottom half of the channel. The channel walls are fixed with flexible plates of length, $l \approx 0.5h$ on the opposite wall. The upstream plate is placed at an entry length of $2h$ from the channel inlet, and the second flexible plate is separated at various distances, i.e., $d = 0h, 0.5h, 1.0h, 1.5h, 2.0h$. The thickness and width of each plate are $b = 0.05h$ and $w = 0.125h$ (into the plane), respectively. The geometry

selected for this study is inspired by our earlier research and a few other similar works Singh and Lakkaraju (2019); Jin et al. (2018), which investigated the flow transition past flexible plates mounted on opposing channel walls. A fully developed flow enters from the left on each dyed half as if the preceding flow had two separate channels with differently dyed fluids Jing and Zhan (2022); ?. The two flow streams in each half enter through the channel and interact with the wall-mounted structures, generating intricate flow features and thereby causing the mixing of the dyed fluids. We have conducted a fluid-structure interaction numerical simulation for the mentioned domain using a partitioned approach, in which the fluid domain and the structure domain are numerically solved separately, and solutions are then exchanged to set iterative boundary conditions at the interface. We have considered fluid as Newtonian and incompressible, mathematically formulated by the Navier-Stokes equations. The linearly elastic structure is framed as solid equations of motion formulated using Arbitrary Lagrangian-Eulerian (ALE) framework Nguyen (2010); Slone et al. (2002); Campbell and Paterson (2011). The mass and momentum conservation expressions for the fluid and the structure are as follows,

$$\nabla \cdot [(\mathbf{u}_f - \mathbf{u}_m)] = 0, \quad (1)$$

$$\frac{\partial \mathbf{u}_f}{\partial t} + [(\mathbf{u}_f - \mathbf{u}_m) \cdot \nabla] \mathbf{u}_f = -\nabla p + \frac{1}{Re} \nabla^2 \mathbf{u}_f \quad (2)$$

$$\rho_s \frac{\partial^2 \mathbf{u}_s}{\partial t^2} = \nabla \cdot \boldsymbol{\sigma}_s \quad (3)$$

Here, $\mathbf{u}_f = (u_x, u_y)$ denotes the flow velocity, while \mathbf{u}_m stands for the moving mesh velocity, and p represents the pressure, ρ_s symbolizes the structure density, \mathbf{u}_s is the structural displacement, t is time, and the Cauchy stress tensor is represented by $\boldsymbol{\sigma}_s$. $\frac{\partial}{\partial t}$ indicates the time derivative operator, and the spatial gradient is defined as $\nabla \equiv \left(\frac{\partial}{\partial x}, \frac{\partial}{\partial y} \right)$, with ∇^2 representing the Laplacian operator. The subscripts f , s , and m refer to fluid, solid, and mesh, respectively.

When the plates deform under the fluid load, the strain rate is expressed as $\boldsymbol{\epsilon}_s = \frac{1}{2} (\nabla \mathbf{u}_s + \nabla \mathbf{u}_s^T + \nabla \mathbf{u}_s \cdot \nabla \mathbf{u}_s^T)$. The relationship between the stress and strain tensors is given by $\boldsymbol{\sigma}_s = 2\mu_s \boldsymbol{\epsilon}_s + \lambda (\nabla \cdot \mathbf{u}_s) \mathcal{I}$, where $\mu_s = \mathcal{E}/[2(1 + \kappa)]$ and $\lambda = \kappa \mathcal{E}/[(1 + \kappa)(1 - 2\kappa)]$ are Lame's constants. Here, κ denotes the Poisson's ratio, \mathcal{E} is Young's modulus, and \mathcal{I} is the identity tensor of rank two. The transpose of a tensor is indicated by the superscript T . The interface condition ensures that flow stress and structural displacement influence each other through no-slip boundary conditions, and the mesh velocity is assumed to be equal to the structure velocity, i.e., $\mathbf{u}_m \equiv \frac{\partial \mathbf{u}_s}{\partial t}$.

In the presented setup, we have added a scalar concentration field ϕ to simulate the dyed fluids effect. The dye concentration fields follow the advection-diffusion equation

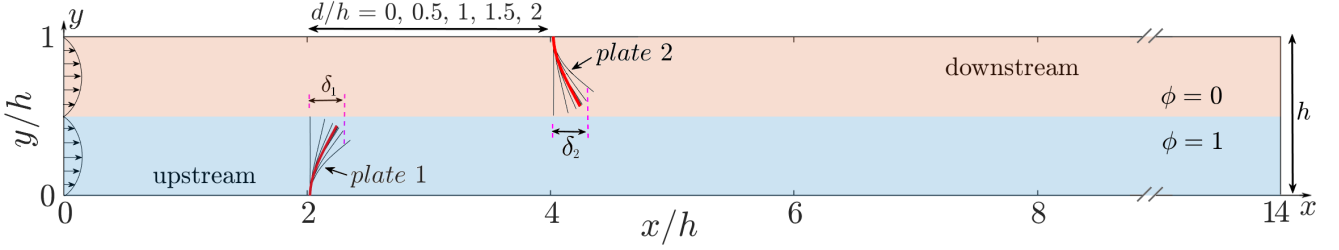


Figure 1: Schematic of a flow in a channel with a scalar concentration field ϕ , separated along the channel length in the top half as $\phi = 0$ and bottom half as $\phi = 1$. The channel walls consist of oppositely mounted flexible plates that bend in the streamwise direction when flow enters from the inlet (left). The inlet flow profile is considered fully developed separately for both the top-half and bottom-half concentration fields as if they enter the domain from two different sources. Plate 1 and plate 2, each of height $0.5h$, are separated at different distances (d/h).

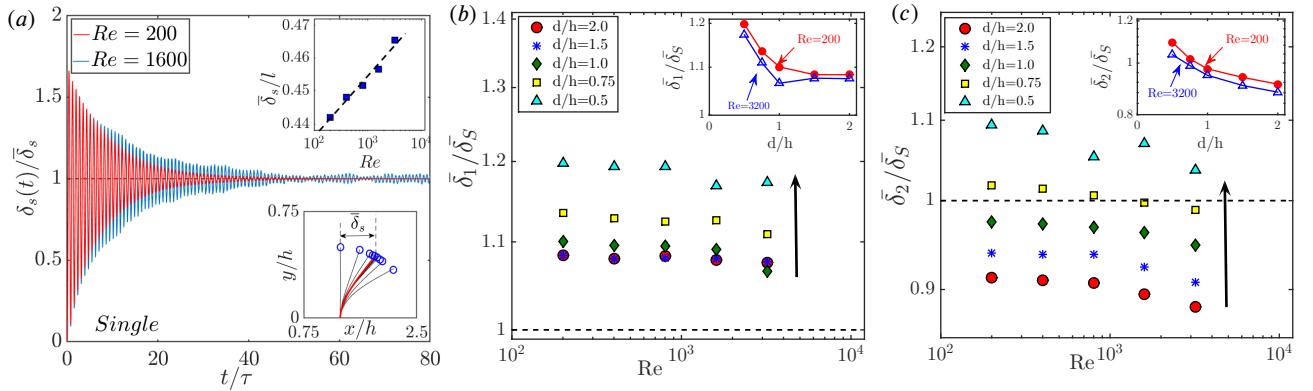


Figure 2: (a) Time history of the single plate tip deflection about steady state mean position for $Re = 200$ and 1600 . A stroboscopic representation of the bending plate is shown in the inset figure, and the thick red plate marks the steady-state shape after deflection. (b) Tip deflection normalized by single plate mean deflection of plate 1 (upstream) and (c) plate 2 for different d/h configurations. The dashed line marks the single plate tip deflection for reference. The inset in each panel shows a tip deflection trend with d/h for $Re = 200$ and 3200 .

as,

$$\frac{\partial \phi}{\partial t} + (\mathbf{u}_f - \mathbf{u}_m) \cdot \nabla \phi = \frac{1}{Re \cdot Sc} \nabla^2 \phi, \quad (4)$$

where ϕ is the scalar concentration field ranging from 0 to 1, and $Sc = v_f/D$ is the Schmidt number with D as the mass diffusivity constant. We used the finite-volume method to solve the mentioned governing equations by employing a second-order accurate Euler-implicit scheme for temporal discretization and a second-order vanLeer TVD scheme for spatial discretization of convection terms. For diffusion terms, we applied a central differencing scheme with Gaussian integration. We maintained the Courant number below 0.2, calculated based on the local velocity magnitude, the integration time step, and the length of the computational cell. Our solution method involves predicting the interface displacement and computing the initial interface residual. This entails estimating the movement of the interface between the fluid and structure domains and determining the deviation from its initial position. After calculating the initial interface residual, the algorithm begins the fluid-structure interaction using a strongly coupled iterative procedure until the convergence criterion is achieved (Tukovic and Jasak, 2007; Campbell and Paterson, 2011). This iterative process

is repeated under the Aitken dynamic relaxation approach until the desired tolerance level is achieved.

In our study, the parabolic inlet profile is expressed as $u_f(y) = 6\bar{U}\left(\frac{2y}{h}\right)\left(1 - \frac{2y}{h}\right)$ for each half separately. Here, \bar{U} is considered as the characteristic velocity and we define the characteristic length as the flow gap between the wall and the wall-mounted plate, which is $(h - l) = 0.5h$ ($= l$). The dimensionless parameters include the Reynolds number $Re = \bar{U}l/v_f$, where v_f ($= \mu_f/\rho_f$), density ratio ρ_s/ρ_f , and Cauchy number as the ratio of fluid inertia to elastic restoring force i.e. $Ca = \rho_f \bar{U}^2 h^3 b / \mathcal{E}I$, where $I = bw^3/12$ is the plate's area moment of inertia (Bagheri et al., 2012; Favier et al., 2015). Another critical parameter is the dimensionless gap between the plates, d/h . Our study primarily involves two time scales: (1) the plate's elasticity time scale, $\tau \sim 1/\sqrt{\mathcal{E}I/(\rho_s b w l^4)}$, and (2) the convective motion time scale, $T \sim l/\bar{U}$. When τ/T is much less than 1, the plate shows oscillations at its natural frequency due to the negligible fluid inertia. Conversely, when τ/T is much greater than 1, fluid inertia dominates the plate's oscillations. Notably, τ and Ca are related through $\tau \sim \sqrt{(\rho_s w/\rho_f h) Ca}$. Given the significance of elastic restoring forces, we selected a

small Ca value (≈ 0.015) to align with previous studies involving flexible silicone obstructions (Vandenbergh et al., 2004; Singh and Lakkaraju, 2019). Our main objective is to examine fluid mixing by varying the inlet Reynolds number within the range $100 < Re < 3200$ and adjusting the plate separation gap from $0h$ to $2h$.

The velocity boundary conditions applied to the channel walls and flexible structure surfaces are no-slip and impermeable. At the channel outlet, we have assumed zero velocity gradient boundary condition. A parabolic profiled inlet from left is supplied for both the top and bottom half to mimic fully developed flow for the two different concentration fields, as previously described. The velocity at the interface between the solid structure and the fluid is the same, i.e., a no-slip boundary condition is used. Pressure boundary conditions are set to zero gradients at the channel walls, inlet, fluid-solid interface, and ambient pressure conditions at the outlet. Our study focuses on the streamwise location $x = 12h$, ensuring no boundary reflections and allowing properties to stabilize before exiting the channel.

3. Results

We have investigated the fluid mixing in a channel flow due to the passively oscillating flexible plates. According to Zhang et al. (2020), such plates subjected to an incoming flow may exhibit different deformation modes: lodging mode, regular VIV mode (vortex-induced vibration or flutter), or static reconfiguration mode. Our parameter range places our cases in the phase space that shows static reconfiguration of the plates, as described in Zhang et al. (2020), where the plates align with the flow, reducing the projected area perpendicular to the flow and showing negligible flutter at steady-state.

To begin with, we studied the behavior of the flexible plates under the incoming flow. In Figure 2(a), we have shown the plates' flutter oscillation for the case where only a single plate is positioned at $2h$ length from the channel inlet. This plate reconfigures by bending in the streamwise direction by amplitude $\bar{\delta}_s$ and flutters around its mean position (shown as plate position in red in the subplot). The plates' flutter amplitude dampens down smoothly for $Re = 200$, unlike that in the high Re ($= 1600$) case where the plates' flutter shows abrupt dampening due to flow features. We have also shown the mean plate deflection for increasing Re in the subplot, which shows a nearly linear trend in the semi-log plot. In the case with two wall-mounted plates arrangement, Figure 2(b) and (c) show steady state deflection amplitude for upstream plate ($\bar{\delta}_1$) and for the downstream plate ($\bar{\delta}_2$) normalized over the deflection amplitude in single plate case ($\bar{\delta}_S$). We can observe that the $\bar{\delta}_1 > \bar{\delta}_S$ for any Re and d/h case whereas $\bar{\delta}_2 > \bar{\delta}_S$ for $d/h > 0.8$. We have also shown the normalized plate deflection for d/h cases in the subfigures and found that the plate deflection increases with a decrease in d/h . We have thoroughly discussed the structural dynamics of the wall-mounted plates' such as

damping, frequency, and deflection, in detail in our earlier work (Singh and Lakkaraju, 2019).

The plates' deflection under the fluid load generates complex flow features due to the mutual interplay of forces. In Figure 3(a), we have shown instantaneous iso-contours of flow vorticity for single plate case at $Re = 200 - 3200$. The flow gets obstructed by the plate and accelerates through the remaining gap, generating vorticity at the top wall and in the form of the plate's tip-attached shear layer. We can notice the roll-up and breakdown of the shear layer upon increasing the Re beyond 200. The clockwise and counter-clockwise vortex structures generated off the plates' tip and the top wall, respectively, arrange themselves in alternating fashion downstream, which indicates periodic shedding of the vortices off the plate. These vortex structures, as they roll, advect downstream due to the incoming inertia and cause a stirring effect in the fluid, thereby causing the mixing of the two fluids.

In Figure 3(b), we have shown two scalar concentration fields $\phi = 0\&1$ initially separated distinctly into top-half and bottom-half, distinctly. For $Re = 200$, the instantaneous scalar field remains largely unmixed due to the flow disturbances as the single plate achieves static reconfiguration mode with negligible flutter amplitude, which does not impact the shear layer breakup. However, for $Re \geq 400$, we can observe a transition in the mixing of the scalar as the aforementioned vortices agitate the field more and more with increasing Re . These vortices entrain the scalar into their field and for localized mixing zones, increasing the mixing by diffusion. In the case with $Re = 3200$, we can note that the flow near the inlet also transitions towards a turbulent field even before interacting with the plates.

The mixing of the scalar field can be statistically evaluated by many methods used in the past (Danckwerts, 1952; Liscinsky et al.; Kockmann et al., 2006). We have used the infamous statistical method for estimating mixing known as the 'Mixing Index', which in our work can be expressed along the channel downstream length as

$$MI(x) = 1 - \sqrt{\frac{\sigma(x)^2}{\sigma_{max}^2}}, \quad (5)$$

$$\text{where, } \sigma(x) = \sqrt{\frac{1}{h} \int_0^h [\phi(x, y) - \phi_m]^2 dy} \quad (6)$$

where $\sigma(x)$ is the standard deviation of the vertically integrated scalar field across the channel, ϕ_m is the mean of the scalar concentration field or scalar concentration value for a fully mixed solution, and σ_{max} is the maximum deviation in the scalar concentration field. According to this method, the 'Mixing Index' ranges from 0 to 1 where $MI = 1$ represents a completely mixed solution and $MI = 0$ represents the fully unmixed scalar field. In our formulation, we have considered the time averaged ϕ in the steady state to diminish any statistical fluctuations. For comparison, we have also

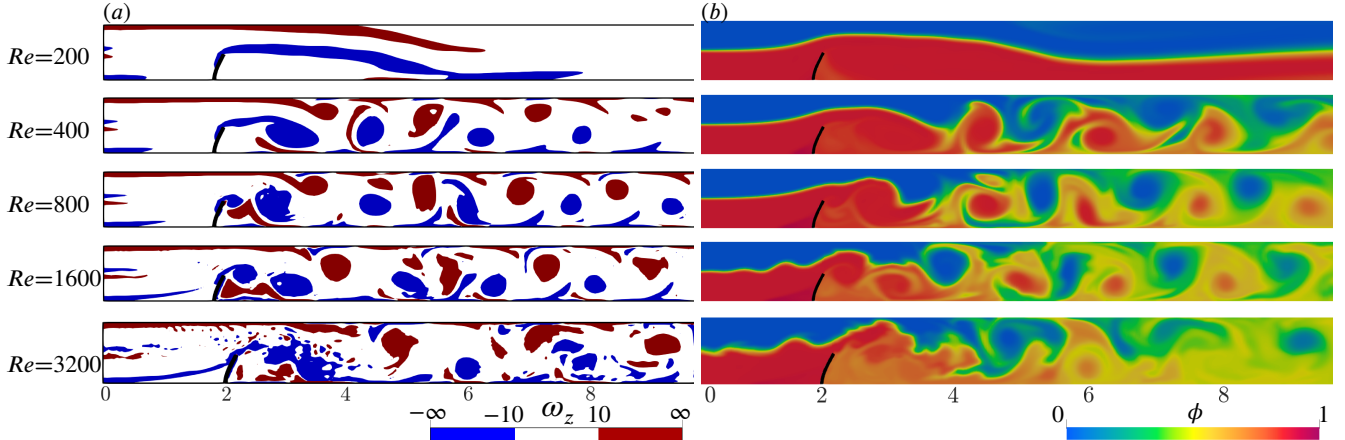


Figure 3: Instantaneous (a) iso-contours of spanwise vorticity (ω_z) and (b) scalar concentration field for single plate configuration case. The top-to-bottom panels are for $Re = 200$ to 3200 .

computed an alternative mixing metric called 'degree of mixing' based on the flux of bulk or cup-mixing average mass fraction as described in Antognoli et al. (2022); Orsi et al. (2013); Galletti et al. (2019). The comparison of these two metrics, presented in Fig. 11(c) in the appendix section, shows consistent trends with our results, differing only by a shift in scale. This shows that the use of time-averaged statistics minimizes the impact of mass flux fluctuations.

We have accounted for a value-for-cost analogy in our work, where MI is considered the final value, which shall come at a cost. We have considered the head loss in the channel flow caused by the presence of flexible obstructions as the cost for the value. We have computed head loss along the channel by vertically (across the channel length) integrating the mechanical head along the channel and subtracting from

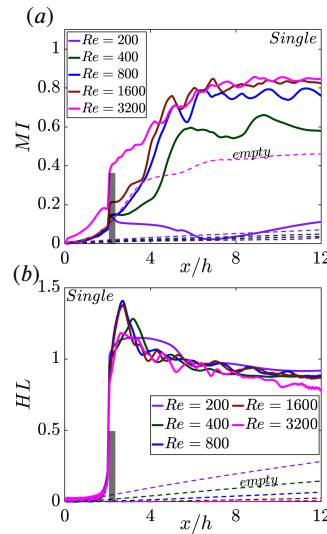


Figure 4: Time-averaged (a) mixing index MI and (b) head loss HL along the channel length downstream for a single flexible plate case for $Re = 200 - 3200$. The grey rectangle marks the location of plates in the channel. The dashed lines correspond to the empty channel case for respective Re as per the color code.

the initial pressure, which is expressed as:

$$\mathcal{H}(x) = \frac{1}{h} \int_0^h [p(x, y) + \frac{1}{2} u_f^2(x, y)] dy; \quad (7)$$

$$\mathcal{H}^*(x) = \frac{\mathcal{H}(x)}{\rho_f \bar{U}^2}; \text{Head Loss, } HL(x) = \mathcal{H}^*(0) - \mathcal{H}^*(x) \quad (8)$$

In Figure 4(a), we show $MI(x)$ for the single plate case for different Re . The grey rectangle in the figure marks the streamwise position of the plate in the channel for reference. As suggested in the contour plots, we see that mixing for $Re = 200$ case is much lower than the higher Re cases. For $Re \geq 400$, the MI shoots high in the channel downstream as early as $x = 5h$. We have also simulated an empty channel flow, i.e., no obstruction, with the same scalar field configuration for the Re range for reference. The dashed curves in the plot show MI for the empty channel case following the same color codes for the Re case. We can notice that the $MI(x)$ in an empty channel follows a linear trend for $Re \leq 1600$, whereas in the case with $Re = 3200$, the flow destabilizes into the transition zone, and a non-linear $MI(x)$ curve can be observed.

In Figure 4(b), we have shown the total mechanical head loss, HL , for a single plate case along the channel streamwise direction for varying Re . The HL spikes up near the plate due to the sudden obstruction of the flow inertia and then decays to a nearly constant value as the flow improves downstream. Despite the difference in MI for varying Re , HL value does not vary significantly with Re near the exit. We have also shown HL for the empty channel case for reference, and an increasing slope in the linear trend can be observed for decreasing Re .

With an initial analysis of the single plate case, we extend our study further by introducing the second plate downstream. In figure 5(a), instantaneous vorticity iso-contours are shown for single and two plate configurations with $d/h = 2, 1.5, 1, 0.5, 0$ at $Re = 400$. The presence of

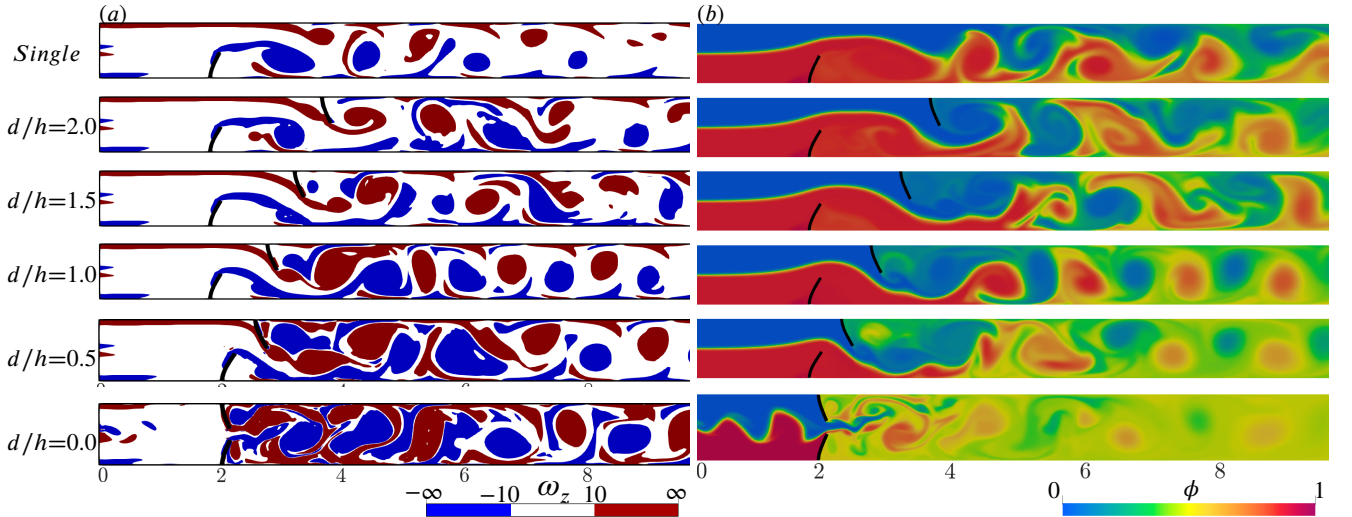


Figure 5: Instantaneous (a) iso-contours of spanwise vorticity (ω_z) and (b) scalar concentration field for $Re = 800$ case. The top-to-bottom panels are for different d/h configurations. A full animation is provided as the supplementary (Animation) for all Re cases.

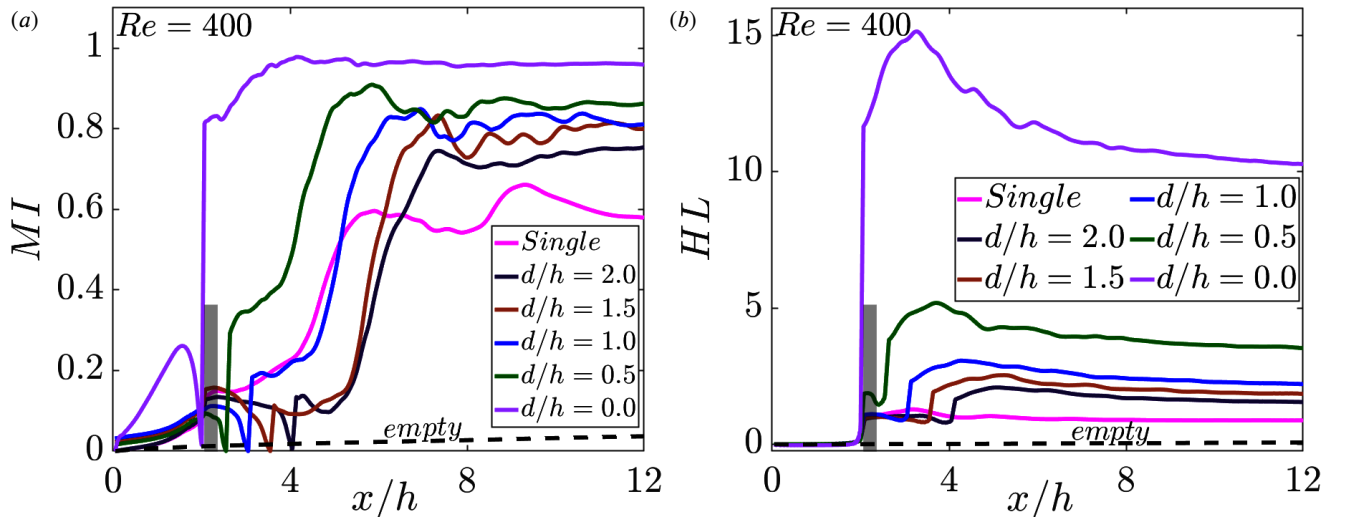


Figure 6: Time-averaged (a) mixing index MI and (b) head loss HL along the channel length in the downstream for single and two plate cases with different d/h configurations at $Re = 400$. The grey rectangle marks the location of plates in the channel. The dashed lines correspond to the empty channel case for respective Re as per the color code.

another plate contributes to more vorticity than the single plate case as plate 2 assists the top wall shear layer to shed periodically of its tip. When plate 2 is placed even closer, the vortex shedding off both plates' tips is more frequent and intense because of its effective flow blockage. In figure 5(b), the instantaneous contour for the scalar field is shown for the same set of configurations at $Re = 800$. In a single plate case, the flow jumps over the plate, destabilizes, and, in turn, agitates further downstream. With the placement of the second plate on the opposite wall, this flow jump gets constricted as per the location of plate 2, and thus, we can notice the early blending of the two fluids as d/h is decreased. Note that, in $d/h = 0$ configuration, the two plates heavily obstruct the flow, disturb the flow even

upstream to the plates, and induce slight fluid mixing before the obstruction.

In Figure 6(a), MI along channel length for the various d/h configurations is compared for $Re = 400$ in steady state. As evident by the contour plots before, the MI in the channel shoots up steeply past the plates' location. The grey rectangle marks the location of plate 1 in the channel for reference. We observe that MI at further downstream locations subsequently decreases with increasing d/h with maximum value at $d/h = 0$, showing significant mixing ahead of the plates and peak mixing immediately next to the plates. However, this steep mixing curve for $d/h = 0$ configuration comes at a high head loss, as shown in figure 6(b), which features a significant difference from the other configurations. The plot shows expected head loss results as

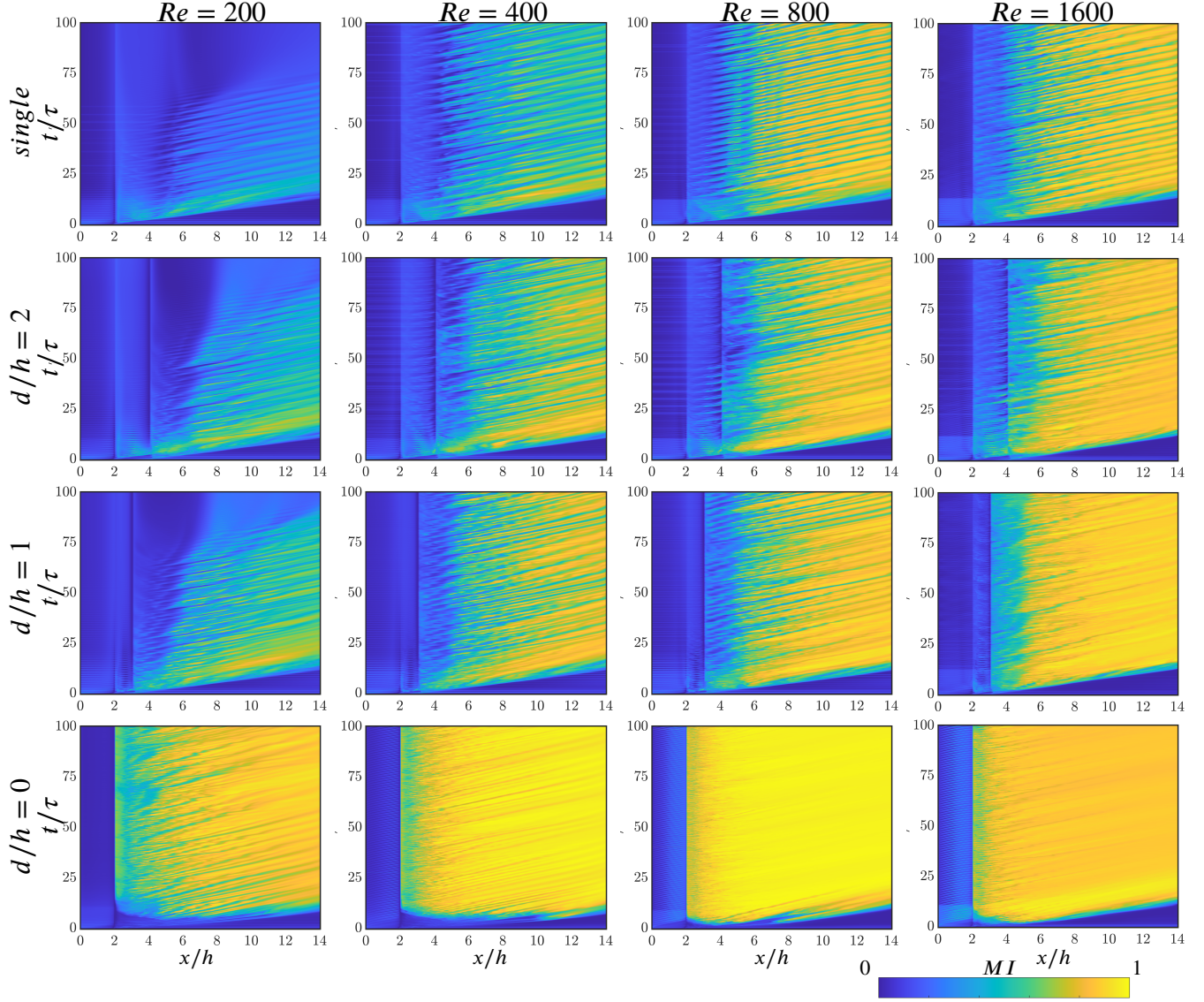


Figure 7: Timespace map for mixing index (*MI*) for single and $d/h = 0, 1, 2$ cases (row-wise), and for $Re = 200, 400, 800, 1600$ cases (column-wise). See animation (Animation) for better understanding.

per the flow obstruction configuration, i.e., decreasing HL with increasing plates' separation (d/h). This result builds on our previous study Singh and Lakkaraju (2019), where we detailed how energy cascades in the flow, measured through energy dissipation rates, and identified intermittent turbulence caused by both the core flow and boundary layers. The stirring effect created by motions at different scales redistributes scalar fields, while molecular diffusion eventually smooths out the gradients at small scales, resulting in thorough mixing. Flow instabilities amplify local fluctuations, increasing the mixing rate. Consistent with our earlier findings, the case with $d/h = 0.0$ shows the highest mixing index (MI), as it also exhibited the highest energy dissipation rates (see Fig. 17 in Singh and Lakkaraju (2019)).

For a comprehensive overview of the development of *MI* for different configurations under various Re , we have shown the time-space plots in figure 7. This reveals that at lower Re , the *MI* increases gradually over time, whereas at

higher Re , we can see early mixing of fluids also increased mixing as the d/h decreases. However, the $d/h = 0$ configuration stands out with the highest mixing very early in the channel as well as early in time. Interestingly, the $Re = 800$ case exhibits much better mixing results than the $Re = 3200$ case for $d/h = 0$.

In Figure 8(a), we have summarised the mixing performance of all the cases studied in our work. We have shown *MI* and *HL* attained at the channel length $x = 12h$ (out of $14h$ length) for cases with different d/h and Re . The data points are clustered according to the Re for each d/h configuration, and the dotted connecting lines are marked only to show the collection and reflect no trend whatsoever. A zoomed-up version of the figure is attached in the Appendix section for details on Re correspondence with the marker point. The data cluster with dark asterisk markers is shown for an empty channel, which results in

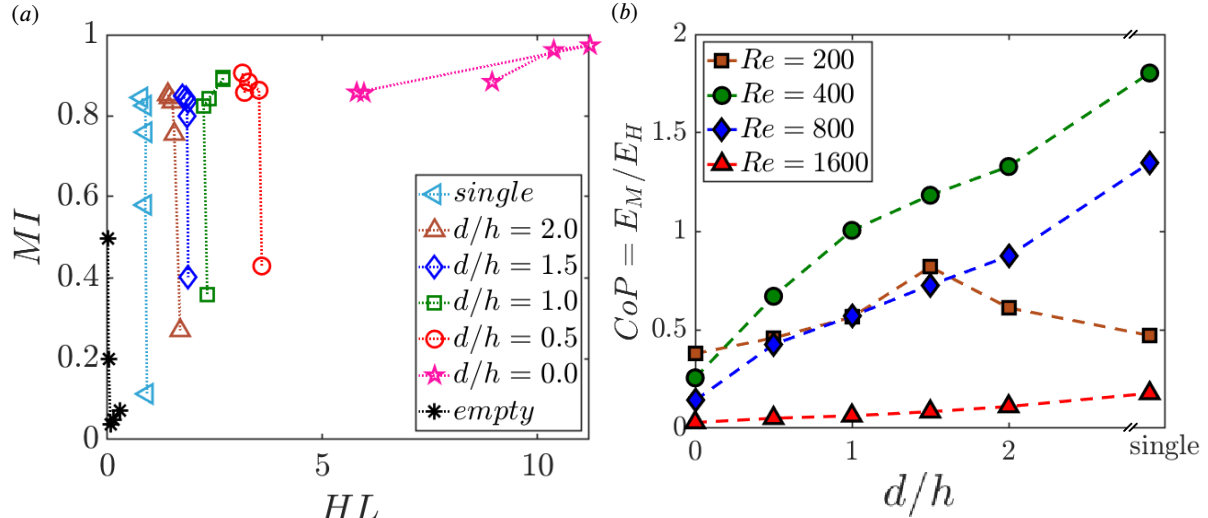


Figure 8: (a) Comprehensive map of all the cases considered in our work in terms of mixing index, MI , and head loss, HL . The asterisk markers correspond to the steady inlet flow case. A zoom-in of each cluster based on the plates' flexibility is shown separately in the Appendix section. (b) Coefficient of performance CoP for different plate configuration cases at $Re = 200 - 1600$.

a reference and relative comparison. The overall data reiterates our finding that the HL increases significantly upon decreasing d/h . However, MI shows results nearly similar for $Re \geq 200$ with $d/h = 0$ case as an exception, which stands out in mixing value but with increased HL as cost.

A key objective when designing a fluid channel mixer is to make it as compact as possible while maintaining adequate mixing. To assess the "compactness" of a channel mixer with wall-mounted plates, we compare it to an empty channel (one without plates) to determine how long the empty channel would need to be to achieve the same level of mixing as the channel with plates at the streamwise location $x/h = 12$. Similarly, we evaluate efficiency losses by finding the length of an empty channel that experiences the same pressure loss as a channel with plates. These equivalent lengths for the empty channel are quantified separately for mixing length (E_M) and head loss (E_H). To estimate these equivalent lengths, we observe that the mixing index and head loss in an empty channel with steady inlet flow (i.e., no plates) can be accurately fit as linear profiles, which for different Re are as:

$$\begin{aligned} Re = 200 &: MI = 0.0015x/h ; HL(x) = 0.0604x/h \\ Re = 400 &: MI = 0.011x/h ; HL(x) = 0.0301x/h \\ Re = 800 &: MI = 0.0082x/h ; HL(x) = 0.0131x/h \\ Re = 1600 &: MI = 0.0024x/h ; HL(x) = 0.0046x/h \end{aligned}$$

Using this information, we introduce a comprehensive evaluation metric as the Coefficient of Performance (CoP) for the mixer, which is calculated as the ratio of equivalent lengths for mixing and the pressure head loss, i.e., $CoP = E_M / E_H$ (Rips and Mittal, 2019; Singh et al., 2024b). This coefficient allows us to measure how much the mixing improves relative to the increase in efficiency loss for a mixer with plates compared to one without any plate. Figure 8(b) shows the CoP for various d/h cases at different flow Re . We find that the CoP increases with d/h with maximum

performance in the case of a single plate in the channel. Also, the plot suggests that the $Re = 400$ allows the best operating conditions for the fluid mixing processes. Notably, at low $Re (= 200)$, plates' configuration with $d/h = 1.5$ serves the best mixing performance.

4. Summary

We conducted numerical simulations to study the mixing in a channel that is set to be filled with fluid of two different scalar concentration fields, which are initially separated along the channel length flow at different Re with a range of $200 - 3200$. We introduced two flexible plates anchored to the channel walls alternately at varying separation distances $d/h = 0, 0.5, 1, 1.5, 2$ and investigated the mixing performance due to the fluid-structure interaction. The flexible plates bend under the flow inertia and oscillate around a mean reconfigured position, which causes vortex shedding off each plate's tip and contributes to the intermixing of the two scalar fields. We used standard metrics to evaluate both the mixing efficiency and the resulting mechanical head loss for the cost-to-value analogy.

Our key findings indicate that the $d/h = 0$ configuration of the two plates in the channel stands out and results in a maximum mixing effect for any Reynolds number category. The mixing, in this case, is also much earlier in the channel, i.e., immediately next to the plates' position and also early in time. However, the plates' arrangement causes maximum obstruction to the flow and thus results in high-pressure head loss. An overall map of the rest of the plate configurations reveals that the decrease in d/h causes the increased head losses but does not contribute to the mixing significantly in flow conditions $Re \geq 400$. To comprehensively assess mixing performance, considering both mixing quality and head loss, we compared our configuration with an empty channel (no obstacles). We used equivalent empty channel lengths

(E_M and E_H) for this comparison, aiming to match the channel metrics with plates. We then calculated the coefficient of performance, defined as $CoP = E_M/E_H$, for all scenarios to rank our setups based on their mixing performance. The highest mixing performance (CoP) is observed for single plate configuration because it features considerably low head loss in the channel flow. We also found that the $Re = 400$ flow condition is best suited for high mixing CoP . At low Re (= 200) in our case, the $d/h = 1.5$ configuration resulted in the highest mixing performance. However, our study has limitations. The channel mixer design used is simple, representing a straight, two-dimensional channel. In practical applications, mixers might feature more complex, duct-like channels where flow dynamics in third dimensions are also important. These three-dimensional aspects could affect the behavior of the elastic plates and overall flow dynamics. Future research could investigate the impact of plate geometry and its placement within the channel on mixing efficiency.

5. Acknowledgement

We sincerely thank the members of the TuRbulent Interfaces and Dispersion (TRIAD) group and the mCFD group at IIT Kharagpur for their unwavering support throughout this work. Our heartfelt gratitude goes to the National Supercomputing Mission and the Param Shakti computing facility at IIT Kharagpur, India, for providing the necessary computational resources. We also extend our appreciation to Dr. Paul Krueger from the University of North Texas for his resource contributions and to Dr. Leixin Ma from the Arizona State University for her valuable insights and engaging discussions.

Appendix

In Figure 9, we show the instantaneous velocity contour (left) and Q-criterion-based vortex structures. The Q-criterion is a method for identifying strong vortices in the flow; Zones dominated by vortices are identified by $Q > 0$, while strained zones are indicated by $Q < 0$ (Kevlahan et al., 1994; Jeong and Hussain, 1995; Holmes et al., 1996; Hemati et al., 2014). We observed that the flow velocity speeds up as the plates' constriction is reduced with decreasing d/h . The compliance of flow with plate 1 and plate 2 causes the flow to meander in a wave-like form downstream. We also observe increasing vortex structures along the channel length with decreasing plates' separation d/h . Figure 10 provides the time evolution of the MI for $Re = 400$ case for different plates' configuration cases. We notice the earliest fluid mixing for the $d/h = 0$ case, whereas the single plate case takes more time to reach its respective MI maximum. In Figure 11(a-b), we zoomed in into clusters of data points shown in figure 8(a) so to better understand the effects of Re on the overall mixing efficiency vs head loss map. In figure 11(c), we have compared our results with an alternative measurement of the mixing which accounts for the mass flux through the cross section as described by Antognoli et al.

(2022); Orsi et al. (2013); Galletti et al. (2019) and termed as 'degree of mixing'. In the figure solid markers represent the 'degree of mixing' approach and show consistent trend with our results but with a shift in scale.

Validation and grid independence

To ensure confidence on our numerical solver, we conducted a validation study where we selected a test case involving a plate oscillating in a fluid flow, as illustrated in Figure 12 of Glück et al. (2001). In Figure 12(a), we present the computed streamwise tip deflection over time and compare it with the results outlined in Section 3.1.2 of Glück et al. (2001). Our simulations showed good agreement with these results. In sequence, we further ensure the accuracy of our results by conducting grid independence results for our study as shown in figure 12(b). We investigated the plates' tip deflection at three different mesh densities and found $\approx 1\%$ difference in the values. Based on the convincing results, we proceeded to simulate all the test cases with the present mesh density. We also tested the results in Fig 10 (in the main manuscript) for $d/h = 1.5$ and $Re = 800$ at different mesh densities to optimize the grid resolution of the scalar field in the domain. We investigated $0.5-1.5 \times$ the presently used mesh to report Mixing Index and corresponding Head Losses and found the saturation of MI and HL results at the used mesh density.

References

- Abdelhamid, T., Alam, M.M., Islam, M., 2021. Heat transfer and flow around cylinder: Effect of corner radius and reynolds number. *Int. J. Heat Mass Transf.* 171, 121105.
- Afzal, A., Kim, K.Y., 2014. Flow and mixing analysis of non-newtonian fluids in straight and serpentine microchannels. *Chemical Engineering Science* 116, 263–274.
- Alben, S., Shelley, M., 2008. Flapping states of a flag in an inviscid fluid: Bistability and the transition to chaos. *Phys. Rev. Lett.* 100, 74301.
- Ali, S., Habchi, C., Menanteau, S., Lemenand, T., Harion, J.L., 2015. Heat transfer and mixing enhancement by free elastic flaps oscillation. *Int. J. Heat Mass Transf.* 85, 250–264.
- Ali, S., Habchi, C., Menanteau, S., Lemenand, T., Harion, J.L., 2017. Three-dimensional numerical study of heat transfer and mixing enhancement in a circular pipe using self-sustained oscillating flexible vorticity generators. *Chemical Engineering Science* 162, 152–174.
- Ali, S., Menanteau, S., Habchi, C., Lemenand, T., Harion, J.L., 2016. Heat transfer and mixing enhancement by using multiple freely oscillating flexible vortex generators. *Appl. Therm. Eng.* 105, 276–289.
- Animation, . Supplementary animation video file URL: <drive.google.com/file/d/1efXQovgV5AGPCEY1zi0in3L6AWyRMd-s>.
- Antognoli, M., Tomasi Masoni, S., Mariotti, A., Mauri, R., Brunazzi, E., Galletti, C., 2022. Investigation on steady regimes in a x-shaped micromixer fed with water and ethanol. *Chemical Engineering Science* 248, 117254.
- Bagheri, S., Mazzino, A., Bottaro, A., 2012. Spontaneous symmetry breaking of a hinged flapping filament generates lift. *Physical Review Letters* 109, 154502.
- Borazjani, I., Sotiropoulos, F., 2009. Vortex-induced vibrations of two cylinders in tandem arrangement in the proximity-wake interference region. *Journal of Fluid Mechanics* 621, 321–364.
- Campbell, R.L., Paterson, E., 2011. Fluid-structure interaction analysis of flexible turbomachinery. *Journal of Fluids and Structures* 27, 1376–1391.

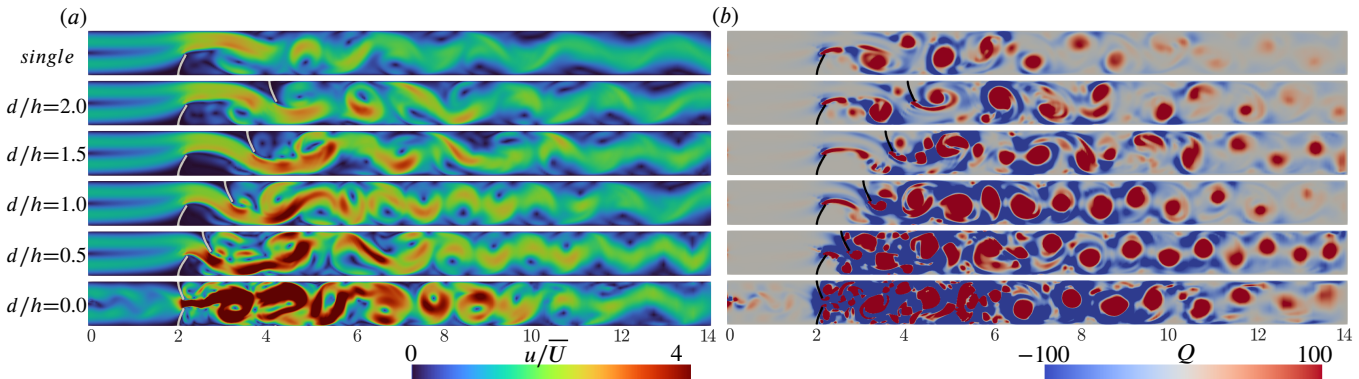


Figure 9: (a) Instantaneous velocity contour for different cases. (b) Q-criterion-based vortex structures are shown. Both cases correspond to $Re = 400$

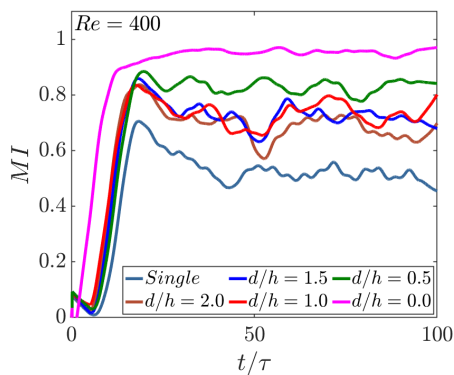


Figure 10: Time evolution of mixing index MI near the channel exit at length $x = 12h$ along the channel length in the downstream for single and two plate case with different d/h configurations at $Re = 400$.

- Chen, Y., Ryu, J., Liu, Y., Sung, H.J., 2020. Flapping dynamics of vertically clamped three-dimensional flexible flags in a poiseuille flow. *Phys. Fluids* (1994) 32, 071905.
- Dadvand, A., Hosseini, S., Aghebatandish, S., Khoo, B.C., 2019. Enhancement of heat and mass transfer in a microchannel via passive oscillation of a flexible vortex generator. *Chemical Engineering Science* 207, 556–580.
- Danckwerts, P.V., 1952. The definition and measurement of some characteristics of mixtures. *Flow Turbulence and Combustion* 3, 279–296.
- Derkzen, J., 2010. Simulations of lateral mixing in cross-channel flow. *Computers & Fluids* 39, 1058–1069.
- Eloy, C., Lagrange, R., Souilliez, C., Schouveiler, L., 2008. Aeroelastic instability of cantilevered flexible plates in uniform flow. *Journal of Fluid Mechanics* 611, 97–106.
- Evegren, P., Revstedt, J., Fuchs, L., 2011. Pulsating flow and mass transfer in an asymmetric system of bifurcations. *Computers & Fluids* 49, 46–61.
- Favier, J., Revell, A., Pinelli, A., 2015. Numerical study of flapping filaments in a uniform fluid flow. *Journal of Fluids and Structures* 53, 26–35.
- Galletti, C., Mariotti, A., Siconolfi, L., Mauri, R., Brunazzi, E., 2019. Numerical investigation of flow regimes in t-shaped micromixers: Benchmark between finite volume and spectral element methods. *The Canadian Journal of Chemical Engineering* 97, 528–541.
- Glück, M., Breuer, M., Durst, F., Halfmann, A., Rank, E., 2001. Computation of fluid-structure interaction on lightweight structures. *Journal of Wind Engineering and Industrial Aerodynamics* 89, 1351–1368.

Grosshans, H., Szász, R.Z., Fuchs, L., 2015. Enhanced liquid–gas mixing due to pulsating injection. *Computers & Fluids* 107, 196–204.

Hemati, M.S., Williams, M.O., Rowley, C.W., 2014. Dynamic mode decomposition for large and streaming datasets. *Physics of Fluids* 26, 111701.

Holmes, P., Lumley, J.L., Berkooz, G., 1996. Turbulence, coherent structures, dynamical systems and symmetry. *Cambridge Monographs on Mechanics* , 20–85.

Hosseini, S., Aghebatandish, S., Dadvand, A., Khoo, B.C., 2021. An immersed boundary-lattice boltzmann method with multi relaxation time for solving flow-induced vibrations of an elastic vortex generator and its effect on heat transfer and mixing. *Chem. Eng. J.* 405, 126652.

Hsiao, K.Y., Wu, C.Y., Huang, Y.T., 2014. Fluid mixing in a microchannel with longitudinal vortex generators. *Chem. Eng. J.* 235, 27–36.

Huera-Huarte, F., Gharib, M., 2011. Vortex- and wake-induced vibrations of a tandem arrangement of two flexible circular cylinders with far wake interference. *Journal of Fluids and Structures* 27, 824–828. IUTAM Symposium on Bluff Body Wakes and Vortex-Induced Vibrations (BBVIV-6).

Jeong, J., Hussain, F., 1995. On the identification of a vortex. *Journal of Fluid Mechanics* 285, 69–94.

Jin, Y., Kim, J.T., Mao, Z., Chamorro, L., 2018. On the couple dynamics of wall-mounted flexible plates in tandem. *Journal of Fluid Mechanics* 852, R2.

Jing, D., Zhan, X., 2022. Numerical studies on the hydraulic and mixing performances of fluid flow around a cylinder in microchannel with vertical flexible flag. *Chem. Eng. J.* 430, 133009.

Kakroo, K., Sadat, H., 2024. High-fidelity fluid–structure interaction simulations of perforated elastic vortex generators. *Physics of Fluids* 36, 113608.

Kang, D., 2015. Effects of baffle configuration on mixing in a T-shaped micro-channel. *Micromachines* 6, 765–777.

Kashid, M., Renken, A., Kiwi-Minsker, L., 2011. Mixing efficiency and energy consumption for five generic microchannel designs. *Chemical Engineering Journal* 167, 436–443.

Kevlahan, N., C. R. Hunt, J., Vassilicos, J., 1994. A comparison of different analytical techniques for identifying structures in turbulence. *Applied Scientific Research* 53, 339–355.

Khatavkar, V.V., Anderson, P.D., den Toonder, J.M.J., Meijer, H.E.H., 2007. Active micromixer based on artificial cilia. *Phys. Fluids* (1994) 19, 083605.

Kockmann, N., Kiefer, T., Engler, M., Woias, P., 2006. Convective mixing and chemical reactions in microchannels with high flow rates. *Sensors and Actuators B: Chemical* 117, 495–508.

Liscinsky, D., True, B., Holdeman, J., . Experimental investigation of crossflow jet mixing in a rectangular duct.

Mehendale, N., Sharma, O., Pandey, S., Paul, D., 2018. Clogging-free continuous operation with whole blood in a radial pillar device (rapid). *Biomedical Microdevices* 20.

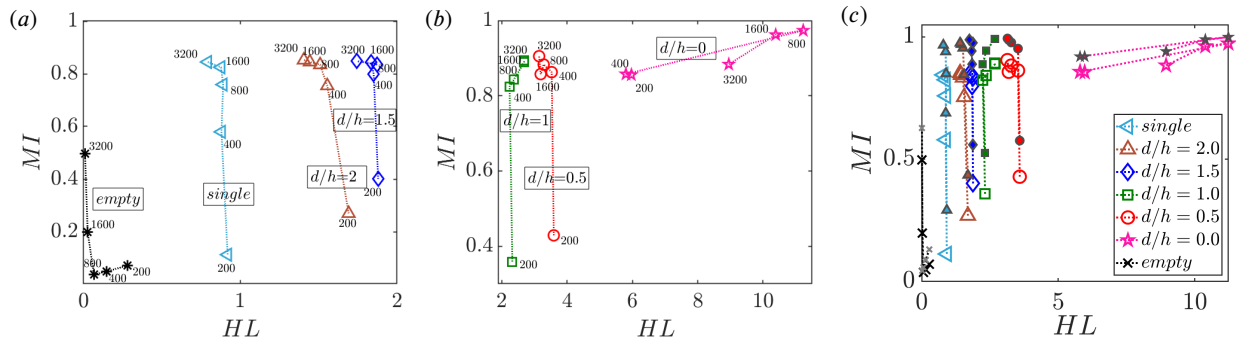


Figure 11: (a-b) Zoom-in of clusters of data points shown in Figure 8(a). Re value is shown near each data point. (c) Comparison of Mixing Index (open markers) and 'degree of mixing' (solid markers) metric for mixing measurements.

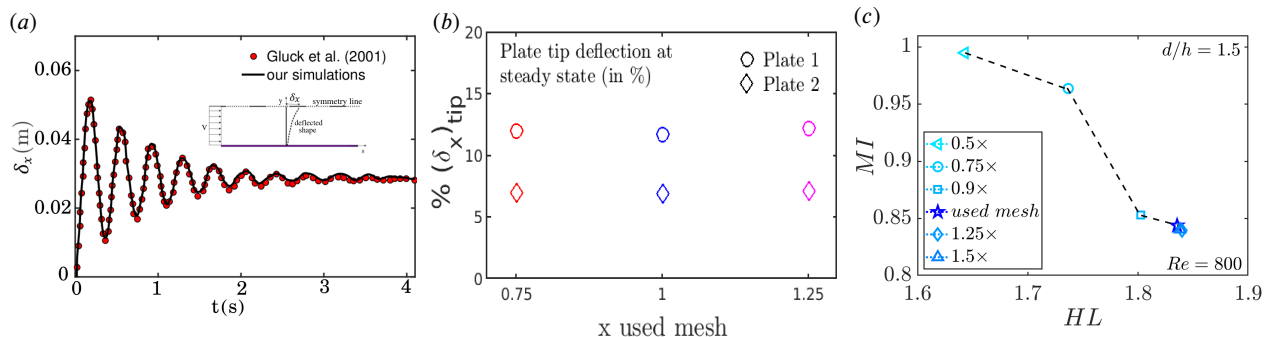


Figure 12: (a) Validation of our results with Gluck et al. (2001). (b) Streamwise tip deflection at 3 different mesh densities (c) MI and HL attained at the channel length $x = 12h$ for cases with $d/h = 1.5$ and $Re = 800$ for different mesh densities.

- Nazari, M., Rashidi, S., Esfahani, J.A., 2020. Effects of flexibility of conductive plate on efficiency of an induced-charge electrokinetic micro-mixer under constant and time-varying electric fields-a comprehensive parametric study. *Chemical Engineering Science* 212, 115335.
- Nguyen, N.T., Wu, Z., 2005. Micromixers—a review. *Journal of Micromechanics and Microengineering* 15, 1–16.
- Nguyen, V.T., 2010. An arbitrary Lagrangian–Eulerian discontinuous Galerkin method for simulations of flows over variable geometries. *Journal of Fluids and Structures* 26, 312–329.
- Núñez-Flores, A., Sandoval, A., Mancilla, E., Hidalgo-Millán, A., Ascanio, G., 2020. Enhancement of photocatalytic degradation of ibuprofen contained in water using a static mixer. *Chem. Eng. Res. Des.* 156, 54–63.
- Orsi, G., Roudgar, M., Brunazzi, E., Galletti, C., Mauri, R., 2013. Water–ethanol mixing in t-shaped microdevices. *Chemical Engineering Science* 95, 174–183.
- Park, J.W., Ryu, J., Sung, H.J., 2019. Effects of the shape of an inverted flag on its flapping dynamics. *Phys. Fluids* (1994) 31, 021904.
- Peterwitz, M., Schembecker, G., 2021. Evaluating the potential for optimization of axial back-mixing in continuous pharmaceutical manufacturing. *Comput. Chem. Eng.* 147, 107251.
- Rips, A., Mittal, R., 2019. Flutter-enhanced mixing in small-scale mixers. *Physics of Fluids* 31, 107107.
- Sadatoshi, T., 1968. Waving motions of flags. *Journal of the Physical Society of Japan* 24, 392–401.
- Saleh, H., Siri, Z., Hashim, I., 2019. Role of fluid-structure interaction in mixed convection from a circular cylinder in a square enclosure with double flexible oscillating fins. *Int. J. Mech. Sci.* 161–162, 105080.
- Singh, G., Lakkaraju, R., 2019. Wall-mounted flexible plates in a two-dimensional channel trigger early flow instabilities. *Phys. Rev. E* 100, 023109.
- Singh, G., Senapati, A., Atta, A., Lakkaraju, R., 2024a. Generating periodic vortex pairs using flexible structures. *Journal of Fluids and Structures* 127, 104126.
- Singh, G., Senapati, A., Sharma, A., Atta, A., Lakkaraju, R., 2024b. Flexible structures enhance fluid mixing in a channel flow. *Physics of Fluids* 36, 024103.
- Slone, A.K., Pericleous, K., Bailey, C., Cross, M., 2002. Dynamic fluid–structure interaction using finite volume unstructured mesh procedures. *Computers & Structures* 80, 371–390.
- Tukovic, Z., Jasak, H., 2007. Updated lagrangian finite volume solver for large deformation dynamic response of elastic body. *Transactions of FAMENA* 31, 55.
- Vandenberghhe, N., Zhang, J., Childress, S., 2004. Symmetry breaking leads to forward flapping flight. *Journal of Fluid Mechanics* 506, 147–155.
- Wang, J., Zhen, Y., 2021. Application and patent of static mixer in plastic processing. *Recent Pat. Mech. Eng.* 14, 94–104.
- Wang, L., Zhou, Y., 2018. Two tandem cylinders of different diameters in cross-flow: Effect of an upstream cylinder on wake dynamics. *Journal of Fluid Mechanics* 836, 5–42.
- Wang, S., Ryu, J., Yang, J., Chen, Y., He, G.Q., Sung, H.J., 2020. Vertically clamped flexible flags in a poiseuille flow. *Phys. Fluids* (1994) 32, 031902.
- Ward, K., Fan, Z.H., 2015. Mixing in microfluidic devices and enhancement methods. *Journal of micromechanics and microengineering: structures, devices, and systems* 25.
- Watanabe, Y., Suzuki, S., Sugihara, M., Sueoka, Y., 2002. An experimental study of paper flutter. *Journal of Fluids and Structures* 16, 529–542.
- Yadav, P.K., Sourav, K., Kumar, D., Sen, S., 2021. Flow around a diamond-section cylinder at low reynolds numbers. *Phys. Fluids* (1994) 33, 053611.
- Yang, A.S., Chuang, F.C., Chen, C.K., Lee, M.H., Chen, S.W., Su, T.L., Yang, Y.C., 2015. A high-performance micromixer using three-dimensional tesla structures for bio-applications. *Chem. Eng. J.* 263, 444–451.

- Yang, J.T., Fang, W.F., Tung, K.Y., 2008. Fluids mixing in devices with connected-groove channels. *Chemical Engineering Science* 63, 1871–1881.
- Yeh, S.I., Sheen, H.J., Yang, J.T., 2015. Chemical reaction and mixing inside a coalesced droplet after a head-on collision. *Microfluid. Nanofluidics* 18, 1355–1363.
- Yu, Y., Liu, Y., Chen, Y., 2017. Vortex dynamics behind a self-oscillating inverted flag placed in a channel flow: Time-resolved particle image velocimetry measurements. *Phys. Fluids* (1994) 29, 125104.
- Zhang, J., Childress, S., Libchaber, A., Shelley, M., 2001. Flexible filaments in a flowing soap film as a model for one-dimensional flags in a two-dimensional wind. *Nature* 408, 835–839.
- Zhang, X., He, G., Zhang, X., 2020. Fluid–structure interactions of single and dual wall-mounted 2d flexible filaments in a laminar boundary layer. *Journal of Fluids and Structures* 92, 102787.
- Zhao, M., 2020. Effects of natural frequency ratio on vortex-induced vibration of a circular cylinder in steady flow. *Phys. Fluids* (1994) 32, 073604.